Rock and Soil Mechanics

Volume 44 | Issue 2 Article 5

4-10-2023

Refined monitoring of the dynamic process of soil desiccation cracking using ERT

Jun-zheng ZHANG
School of Earth Sciences and Engineering, Nanjing University, Nanjing, Jiangsu 210023, China

Chao-sheng TANG
School of Earth Sciences and Engineering, Nanjing University, Nanjing, Jiangsu 210023, China

Xue-peng GONG
School of Earth Sciences and Engineering, Nanjing University, Nanjing, Jiangsu 210023, China

Qi-you ZHOU
School of Earth Sciences and Engineering, Nanjing University, Nanjing, Jiangsu 210023, China

See next page for additional authors

Refined monitoring of the dynamic process of soil desiccation cracking using ERT

Authors

Jun-zheng ZHANG, Chao-sheng TANG, Xue-peng GONG, Qi-you ZHOU, Qing CHENG, and SHI Bin LÜ Chao

Rock and Soil Mechanics 2023 44(2): 392−402 ISSN 1000−7598
https: //doi.org/10.16285/j.rsm.2022.5409 http://rocksoilmech.researchcommons.org/journal

Refined monitoring of the dynamic process of soil desiccation cracking using ERT

ZHANG Jun-zheng, TANG Chao-sheng, GONG Xue-peng, ZHOU Qi-you, CHENG Qing, LÜ Chao, SHI Bin

School of Earth Sciences and Engineering, Nanjing University, Nanjing, Jiangsu 210023, China

Abstract: Desiccation cracking of soil affected by actions of climate is a common phenomenon in nature. The presence of cracks can dramatically weaken the engineering properties of soil and cause many geotechnical and geological engineering problems. In this study, a refined monitoring method of the dynamic process of soil desiccation cracking using electrical resistivity tomography (ERT) was proposed to determine the development of the cracking networks in clayey soil. The model test and in-situ test were carried out to monitor the process of soil cracking separately. Self-developed resistance measuring system was applied to continuously collecting the current-potential difference data. The data were then processed and inverted using a self-developed system named FemERT (finite element method electrical resistivity tomography) to obtain spatial distribution characteristics of the cracking networks at different periods. The results show that: (1) ERT can achieve the refined monitoring of the soil cracking process and can monitor the geometric morphology of three-dimensional crack networks. The identification accuracy of crack width and depth can reach millimeter level and centimeter level respectively. (2) The difference in sensitivity distribution of ERT can explain the influence of cracking on soil resistivity. The measured resistance curves show different features according to the position of the crack formatting. (3) The interpreted resistivity and its relative change rate (Rev) can directly describe the spatial geometric morphology of the cracking networks at different stages, highlighting the influence of the dynamic development process of cracking on the electrical conductivity of soils.

Keywords: soil desiccation cracking; electrical resistivity tomography (ERT); soil resistivity; crack characterization; crack monitoring; crack propagation process

1 Introduction

Climate change has become one of the major global concerns since the 21st century. Its impacts include not only global anomalies in climate conditions, but also the occurrence of extreme climate events in local areas[1]. With a wide area and diverse climatic phenomena, China is more likely to be exposed to various extreme climate events, such as extreme dry, wet, cold, and hot climates. Under the influence of arid climate or dry–wet climate cycle, plenty of desiccation cracks are easily developed in the clayey soil in nature, which greatly weakens the engineering properties of soils and induces diverse geological disasters such as landslide, landfill leakage, deformation and cracking of subgrade, and tilt and destruction of buildings[2–4], bringing serious threat to the life and property of the public, and causing considerable concerns in the field of geotechnical and geological engineering.

Shrinkage and desiccation cracking process of soils has been studied extensively in recent years[5–7]. For example, Alonso et al.[8] found that soil shrinkage consists of macrostructural elastic deformation and microstructural deformation through soil drying tests under controlled-suction conditions. Tang et al.[9] believed that suction and tensile strength are the key mechanical parameters to control soil desiccation cracking which is essentially a type of tensile failure. Obtaining the geometric parameters during crack development has been the focus of soil cracking studies[10–13], usually through three methods: laboratory test, field observation, and numerical simulation[14]. However, these methods have their shortcomings or difficulties. For instance, photography and digital image processing techniques are often used in laboratory tests to obtain the information about the soil surface cracking, with low cost and high efficiency[15–16]. However, it is easy to be interfered by many factors such as surface cover conditions and lighting, and thus the cracks cannot be detected inside soils. The conventional manual excavation to observe in situ soil cracks is laborious, inaccurate and can cause irreversible damage to soils[17]. Numerical approach can be used to predict the three-dimensional (3D) crack networks, but due to the immature studies on the soil desiccation cracking mechanism and theories, setting evaporation boundary conditions and selecting soil properties parameters face many uncertainties, and the crack network obtained from the numerical simulation present large discrepancies from reality[18]. Furthermore, some monitoring techniques have been used extensively, including X-ray computed tomography (CT)[19], laser scanning[20], distributed optical fiber sensing

Received: 31 March 2022 Accepted: 18 June 2022
This work was supported by the National Science Foundation for Outstanding Young Scholars (41925012), the Key Program of National Natural Science Foundation of China (42230710), the National Key Research and Development Program of China (2019YFC1509902, 2020YFC1808101) and the Natural Science Foundation of Jiangsu Province (BK20211087).
First author: ZHANG Jun-zheng, male, born in 1999, PhD candidate, research interests: environmental geotechnical engineering and high-density electrical resistivity method. E-mail: zhangjunzheng@smail.nju.edu.cn
Corresponding author: TANG Chao-sheng, male, born in 1980, PhD, Professor, research interests: environmental geotechnical engineering and engineering geology. E-mail: tangchaosheng@nju.edu.cn

technique[21] and high-density electrical resistivity tomography (ERT)[22–27]. As a non-destructive geophysical monitoring method, ERT has the advantages of high accuracy, low cost and simple operation, and can realize continuous monitoring in time and space. It is widely used in many fields including geological survey[28], slope monitoring[29], agricultural survey[30], archaeological excavation[31] and engineering construction[32]. Moreover, ERT is extremely sensitive to the distribution of moisture field[33], which is theoretically more suitable for the study of soil desiccation cracking due to evaporative water loss.

Some studies have attempted to use ERT for soil crack monitoring. For instance, Samouëlian et al.[22] employed the two-dimensional ERT to monitor artificial cracks and found that cracks can cause resistivity changes. Sentenac et al.[23] carried out desiccation cracking tests in clayey soils and obtained the similar results. Jones et al.[24–25] conducted the 3D ERT detection of desiccation cracks in laboratory and in situ soils. Tang et al.[26] and An et al.[27] discussed the correlations between the apparent resistivity and crack parameters. Some scholars also analyzed changes of resistivity or resistivity anisotropy of cracked soils with consideration of the geometric morphology of different cracks[34–37]. Although the preliminary investigation has been carried out on this topic, the monitoring of soil cracking by ERT is currently only applicable to roughly monitoring cracks at the centimeter scale or larger due to the accuracy limitation. In addition, few studies have continuously monitored the initiation and propagation of crack networks, ignoring the specific effects of crack dynamic development on soil conductivity. Therefore, a set of refined monitoring method and data processing solution based on ERT is urgently needed to evaluate the geometric morphology and dynamic development of cracks in more details.

In this study, a self-developed system was adopted to set up an ERT monitoring method including electrode fabrication, data acquisition, pre-processing, and inversion to realize the dynamic and refined monitoring on the formation and development of crack network during the drying process of clayey soil. The cracking processes of the model and the in situ soils were monitored to explore the influence of crack development on the testing electrical resistance and to obtain the dynamic development characteristics of crack networks, which are expected to provide new ideas and technical references for evaluating the crack development of soils in practical engineering.

2 Experimental plan

2.1 Laboratory model test

2.1.1 Materials and specimen preparation

The soil selected for this test was taken from 0.5 to 1.0 m below the ground level in Ningzhen area (the water table is about 3 m below the ground level), which is called Xiashu soil. Its physical properties are listed in Table 1. The specimen was prepared in the following procedure: (1) The soil was air-dried, crushed and then passed through a 2 mm sieve. Its air-dried moisture content was 6.6%. (2) The inner wall of the specially prepared mold with a size of 40 cm×30cm× 25 cm was coated with a layer of Vaseline to ensure the free detachment and shrinkage of the soil when cracking. (3) The air-dried soil was divided into four equal parts. They were put into the mold in turn and compacted in layers, with thickness of 5 cm each layer. The final compacted soil specimen has the size of 40 cm×30 cm×20 cm and a dry density of 1.4 g/cm^3. (4) The specimen was humidified with water added to the soil surface slowly. The air vent at the bottom of the mold was kept open so that the gas inside the soil can be expelled during wetting. (5) The wetting process continued until water accumulated on the soil surface. After that, adding water was stopped and the air vent was closed, and the specimen stood for 24 h to ensure the soil pore water distributed evenly. Then the excess water on the soil surface was removed and the specimen preparation was completed.

Table 1 Physical properties of Xiashu soil

Specific gravity G_s	Liquid limit w_L /%	Plastic limit w_P /%	Plastic index I_p	Maximum dry density ρ_d /(g • cm^{-3})	Optimum moisture content w_{opt} /%
2.73	36.5	19.5	17.6	1.71	15.7

2.1.2 ERT monitoring during test

Digital image acquisition and ERT monitoring were carried out simultaneously (Fig. 1(a)) to monitor the cracking process during soil drying in real time. The camera was mounted over the mold to take pictures of the surface soil. Sixty four miniature electrodes, fabricated using lead bolts with a diameter of 2 mm and a length of 8 mm, were inserted from the soil surface in the form of an 8 × 8 square array, with the spacing between the adjacent electrodes approximately 4 cm (Fig. 1(b)). In this way, the satisfactory contact and electrical conductivity between the electrodes and the soil can be achieved, while the development of cracks during ERT monitoring will not be affected. To accelerate soil cracking, a fan was set up on one side of the mold to promote moisture evaporation and the ambient temperature was maintained at 25 °C. Digital image acquisition and resistance measurement were conducted simultaneously with a monitoring interval of 1 h and the whole experiment continued for 63 h.

The equipment used is the self-developed system named “ERT21”, which can realize any fast switching of 128 channels and is a 3D high-density resistivity measurement system for multi-scale targets. The standard four-electrode array for measuring resistivity was adopted, and Wenner array was employed (Fig. 1(c)) due to its good quality of acquiring signals, the ease of data analysis, and the survey line direction including two orthogonal directions and their diagonals, which fully covers the soil surface (Fig. 1(b)). In a single test, 162 sets of current and potential difference can be collected, with an acquisition time of approximately 10 min.

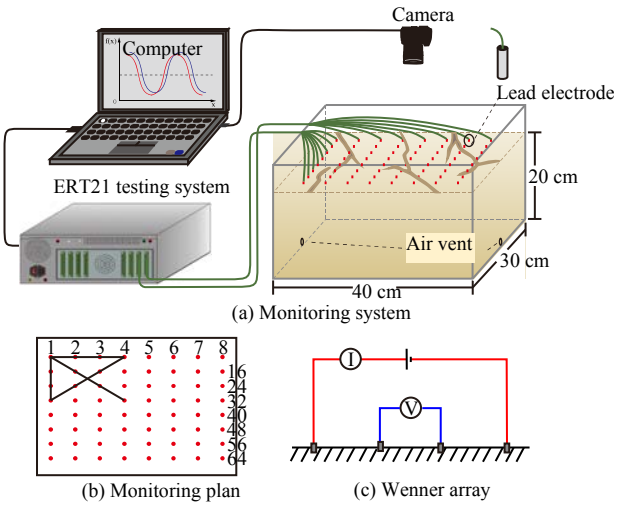

Fig. 1 Illustration of the laboratory test and ERT testing method

2.1.3 Data processing and inversion

The raw data obtained by ERT21 system are the current I and the potential difference $\Delta\Phi$ from different electrode arrays. To determine the resistivity distribution inside the specimen, the raw data are subjected to preliminary screening, apparent resistivity calculation and inversion. A total of 162 sets of the I– $\Delta\Phi$ were substituted into Ohm's law to obtain the measured resistance R of different electrode arrays:

$$R = \frac{\Delta\Phi}{I} \tag{1}$$

Then the measured resistance values of one specific electrode array at different times were compared to exclude the unreasonable maximum and minimum values. The filtered resistance values can be calculated as the apparent resistivity by the following formula:

$$\rho_a = 2\pi aR \tag{2}$$

where a is the test spacing of the Wenner array. The 157 measured resistance values after screening can be used to calculate the 3D distributed data points of apparent resistivity. The horizontal position of each data point corresponds to the center of the electrode array, and its depth is equal to the test spacing of the corresponding electrode array a. The calculation result of a specific measurement is selected here to visually display the apparent resistivity whose projection on the horizontal plane is shown in Fig. 2(a).

The apparent resistivity actually reflects the electrical conductivity of the medium within a certain range around the corresponding electrode array, rather than the actual resistivity of the place where the data point is located. To obtain more actual resistivity distribution, the interpolation data of the apparent resistivity are used as the initial model, with the self-developed system named FemERT for inversion calculation. FemERT is a Linux-based resistivity imaging data processing system with various functions such as mesh generation, sensitivity analysis, forward calculation, inverse calculation, and data analysis. The inversion algorithm used in FemERT is a patching method based on the finite element method[38–39], which minimizes the voltage error and obtains an interpreted resistivity model close to the actual conditions by comparing the simulated voltage with the measured voltage and correcting the initial resistivity model interpolated from the apparent resistivity gradually. The FemERT system has been successfully applied in many studies[33, 40–41]. The inversion calculation in this study was carried out based on the hexahedral elements, with edge length of 2 cm and a total of 20×15×10=3 000 elements (Fig. 2(b)). The final root mean square decrease (RMSD) of the errors between the simulated and measured voltages was controlled within 5% after eight times of inversion and iterative calculation for the data in each test. The final interpreted resistivity model was the 3D distributed resistivity data. The inversion result from one measurement was chosen here, and the top layer data (1 cm) of the model was intercepted to show the interpreted resistivity image (Fig. 2(c)).

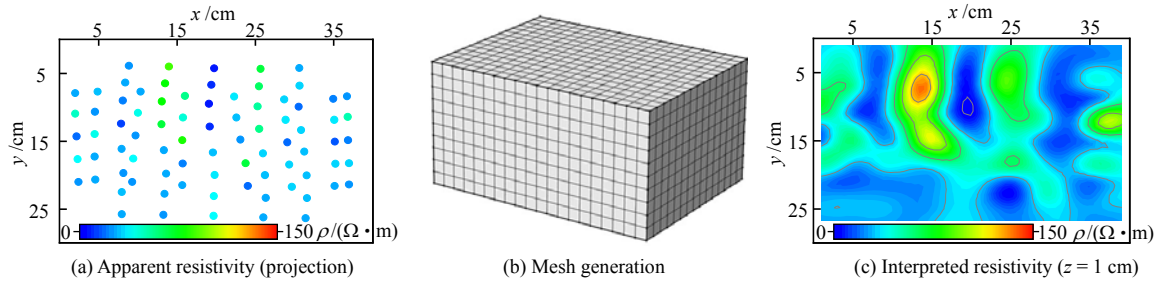

Fig. 2 Process of data processing and inversion

2.2 Field test

2.2.1 Site selection and treatment

The field test site was located within the Xianlin campus of Nanjing University, where the soil belonged to Xiashu soil type. A square test area of 1 m × 1 m was levelled before the test with the surface vegetation and impurities cleared. The test area was watered until the surface was waterlogged and then watered again after the water had infiltrated, which was repeated five times so that the shallow surface soil was fully wetted (Fig. 3(a)).

2.2.2 Test procedure and ERT monitoring

Sixty four aforementioned miniature lead electrodes were placed in a square area of 49 cm×49 cm in the form of square array which is the same as the layout in the laboratory model tests (Fig. 1(b)), with a distance between the adjacent electrodes of 7 cm. It was

difficult for desiccation cracks to develop under natural dry conditions due to the dense soil at the site. Therefore, after the completion of the electrode placement, three simulated cracks were manually created in stages according to the following steps (Fig. 3(b)): (1) stage A: crack I with 49 cm long and 3 cm deep was created by inserting a steel plate of 3 mm thick into the soil (Fig. 3(c)); (2) stage B: the 7–41 cm segment of crack I was deepened to 6 cm (Fig. 3(d)); (3) stage C: the 24–41 cm segment of crack I was deepened to 9 cm (Fig. 3(e)); (4) stage D: the 32–41 cm segment of crack I was deepened to 12 cm (Fig. 3(f)); (5) stage E: the steel plate was inserted into the soil to create crack II which was 23 cm long and 3 cm deep (Fig. 3(g)); and (6) stage F: crack II was lengthened, and crack III with a depth of 3 cm was created (Fig. 3(h)). All cracks were 3 mm wide.

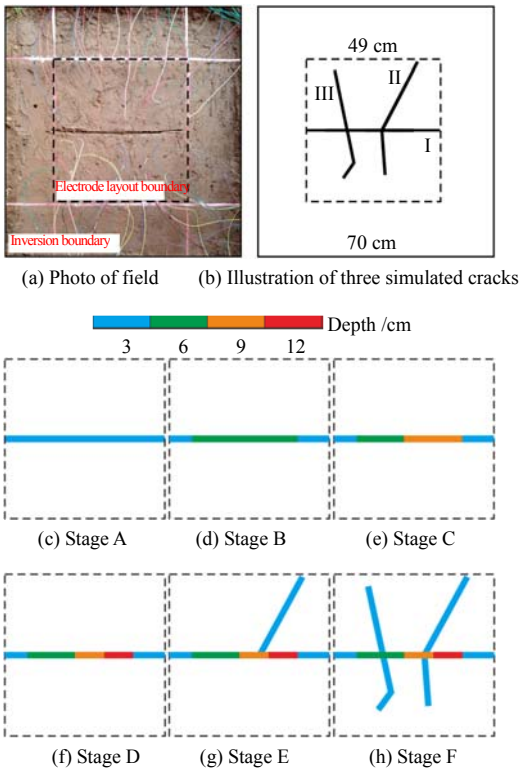

(a) Photo of field (b) Illustration of three simulated cracks

(c) Stage A (d) Stage B (e) Stage C

(f) Stage D (g) Stage E (h) Stage F

Fig. 3 Photo of field and illustrations of artificial cracks

High-density ERT was used for soil measurements in the pre-test crack-free phase and six artificially simulated cracking phases, with the Wenner array for ERT apparatus. There were 162 sets of current–potential difference data obtained from one single measurement. The preliminary screening and the inversion of the raw data were the same as those for the laboratory model tests. No boundary correction based on the current source mirror was performed as the target body of the field tests is approximately semi-infinite space. Due to differences in the size of the study area and the electrode spacing, the inversion was carried out for a size of 70 cm×70 cm×35 cm, with uniform hexahedral meshing in finite element model. A total of 30×30×15=13 500 elements was obtained and the side length for each element is 2.333 cm. The number of iterations and error control methods are the same as those used in the laboratory model tests.

3 Results and analysis

3.1 Desiccation cracking process of laboratory soils and characteristics of time–resistance curve

The digital image acquisition, carried out in parallel with the drying of the soil, accurately recorded the formation and development of cracks. Figure 4 shows that at 18 h of drying, one crack first forms from the top of the image (Fig. 4(b)) and then develops downwards; after 20 h of drying, several cracks develop successively (Figs. 4(d)–4(g)); and finally at 30 h, a basically complete crack network is formed (Fig. 4(h)). The digital images also qualitatively recorded the changes in soil moisture content distribution. The soil in the upper part of the image lost moisture faster due to the fan, which is shown in the images as the lighter-colored soil (Fig. 4(c)). Thereafter, as the cracks propagate, the lighter-colored area also extends downwards with the cracks (Figs. 4(d)–4(h)). This reflects the rapid decrease in moisture content of the surface soil first from the upper part of the image and then extending downwards until the overall stabilization.

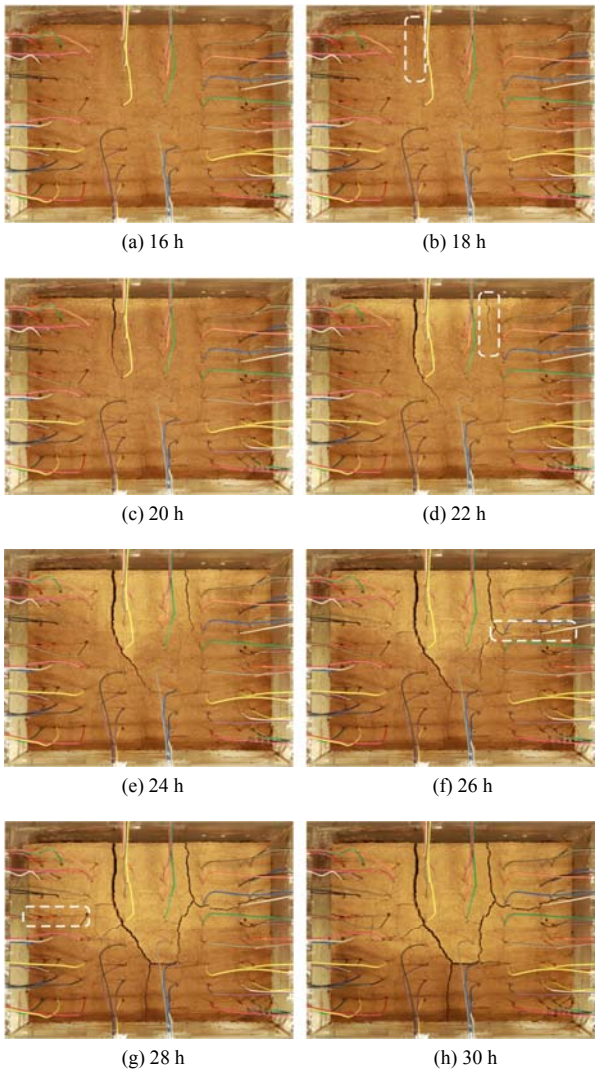

(a) 16 h (b) 18 h

(c) 20 h (d) 22 h

(e) 24 h (f) 26 h

(g) 28 h (h) 30 h

Fig. 4 Photos of the crack network during drying

The electrode arrays are divided into four types according to their positions in relation to the crack network to analyze the influences of the crack formation and development on the electrical conductivity of soils (Fig. 5): (1) cross-crack array, where the crack passes between two potential electrodes (MN); (2) separation array, where the crack passes between the current electrode and the adjacent potential electrode (AM or BN); (3) along-crack array, where the crack is basically parallel to the survey line of the electrode array and does not pass between the electrodes; and (4) others, where the crack propagates to the position of the electrode, or where multiple cracks coalesce on a single electrode array. The resistance measured at different times for an electrode array is influenced by the crack development process, so that the curve of the measured resistance values with time can be plotted. Due to space limitations, this paper focuses on the analysis of the measured resistance curves of the first three electrode arrays, and investigates the influence characteristics of the measured resistance in the process of crack development.

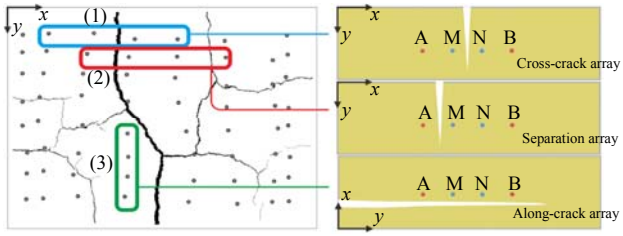

Fig. 5 Classification of different electrode arrays

3.1.1 Resistance–time curves of cross-crack array

According to the measurement principle of standard four-electrode array, when a crack just passes between two potential electrodes, the current field between the current electrodes will inevitably change, which will affect the current–potential difference data obtained from the test. Figures 6(a)–6(c) show that the longitudinal crack crosses array 1 at 18 h after the start of the test (Fig. 6(a)), array 2 and array 3 at 19 h (Fig. 6(b)), and array 4 at 20 h (Fig. 6(c)). These time points match well with the time of the rising inflection points of the resistance curves for each array, indicating that the crack development increases the measured resistance of the cross-crack arrays at different positions, and the specific times can be accurately reflected by the resistance–time curve. Figure 6(d) shows the change of measured resistance with elapsed time for several typical cross-crack arrays. It can be found that all curves turn from relatively stable to an apparently upward trend at a specific time point (the solid point of the curve).

The detection capability of the high-density electrical resistivity method is closely related to the electrode array selected for testing. The sensing capability of different electrode arrays varies. The distribution of the sensing capability of an electrode array in different areas around it can be acquired by numerical simulations, called the sensitivity distribution[42]. The measured potential difference will increase when a high-resistivity body is placed in a high-sensitivity zone, whereas the potential difference measured will decrease when a high-resistivity body is presented in a negative-sensitivity zone, hence an appropriate electrode array should be selected to satisfy different test purposes. The Wenner array adopted in this study has a strong sensing capability for the zone between the two potential electrodes (MN); however, there is a negative sensitivity zone between the current electrode and the potential electrodes (AM, BN). As shown in the contour map of the sensitivity distribution of the Wenner array in Fig. 6(e), the crack as a high-resistivity body blocking the current passes through the high sensitivity zone (red zone) between the electrodes (white dots), making the potential difference of the corresponding electrode array increase, i.e. the measured electrical resistance value rises significantly. Ignoring the causes of this simple phenomenon may lead to misinterpretation of the data, as will be explained in the next subsection.

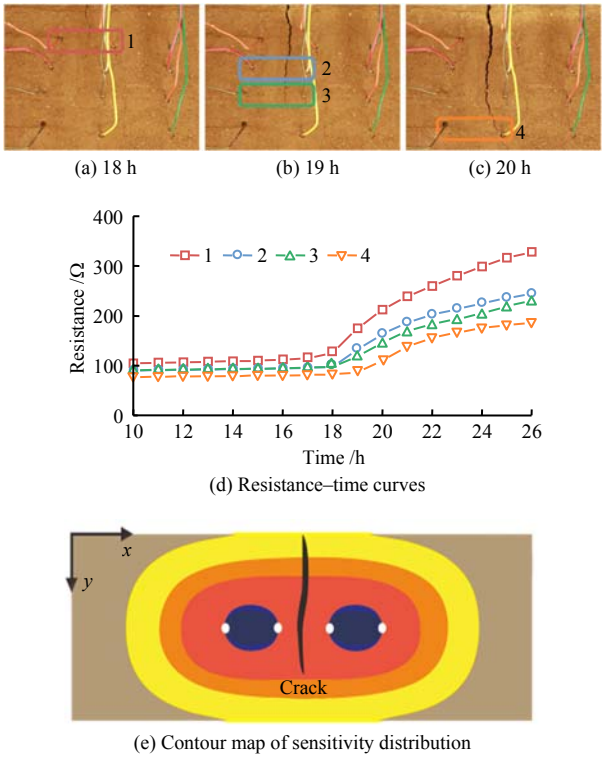

Fig. 6 Photos of the cross-crack array, corresponding resistance curves and contour map of sensitivity distribution

3.1.2 Resistance–time curves of separation array

In contrast to the resistance–time curves of cross-crack array, there is a decreasing inflection point in the resistance curves of the separation array during the crack development, and the time corresponding to the inflection points is also basically consistent with the time when the crack crosses the electrode survey line (Fig. 7(a)–7(c)). Figure 7(d) shows the variation of the measured resistance with time for several separation arrays. According to the sensitivity distribution theory,

the crack as a high-resistivity body appears in the negative-sensitivity zone (the blue area) when it propagates between the current and potential electrodes of the separation array (Fig. 7(e)), causing a decrease in the measured resistance. This phenomenon is known as an "anomaly inversion"[42]. The non-uniformity of the sensitivity field is the cause of the different feedbacks when the crack passes through different electrode arrays (or different locations of the electrode arrays), because the crack propagation can be regarded as a continuous extension of the high-resistivity body.

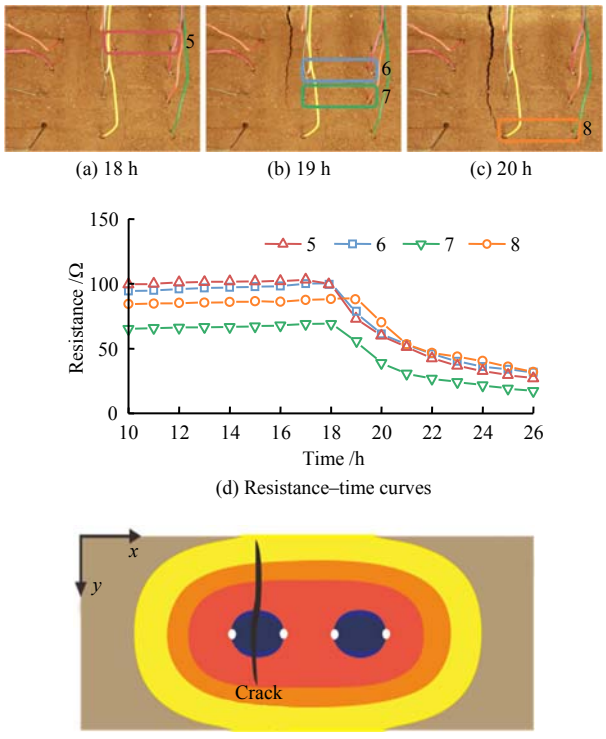

Fig. 7 Photos of the separation array, corresponding resistance curves and contour map of sensitivity distribution

Using ERT to monitor complex and variable desiccation crack networks is bound to produce anomaly inversions; however, most of the existing studies have ignored this problem, which may not have much impact on monitoring the geometric distribution of crack network. Researchers can still describe the development of the crack network by the appearance of high-resistivity anomaly zones and ignore the presence of low-resistivity anomaly zones. However, ERT is also sensitive to the moisture field, and studies have been carried out on the distribution and migration of pore water in fissured soils[43–44]. If the anomaly inversion caused by the presence of cracks is not considered, the distribution of the moisture field may be misjudged; hence it is worth investigating how to reduce the interference of cracks with ERT monitoring.

3.1.3 Resistance–time curves of along-crack array

The measured resistance curve of the electrode array also shows a rising inflection point during the crack development when the crack does not pass between any two electrodes of an electrode array but propagates in a direction almost parallel to the survey line of the array (Fig. 8). The two along-crack arrays in the figure are affected by two different cracks: the left longitudinal crack is close to array 9 at 19 h (Fig. 8(a)) and the resistance curve of array 9 shows a clear rising inflection point at this time, while the right longitudinal crack is close to array 10 at about 23 h (Fig. 8(c)) and the resistance curve of array 10 has a rising trend, but the inflection point is not obvious. The influence of crack development in the along-crack array can still be explained by the sensitivity distribution. The cracks still appear as high-resistivity bodies in the high-sensitivity zone around the electrode array even though they do not cross the survey line (Fig. 8(e)), thus increasing the measured resistivity values. In addition, differences in moisture content due to non-uniform water loss may also be responsible for the increase of the measured resistance. The change of the dashed lines marked in Fig. 8(a)–8(c) reflects the advancing process of the relatively dry and wet interface. According to Archie's law[45], the lower the degree of saturation for the porous medium is, the higher the resistivity will be. However, it is believed that change in soil moisture content has less influence on the measurement of resistivity compared with desiccation cracks.

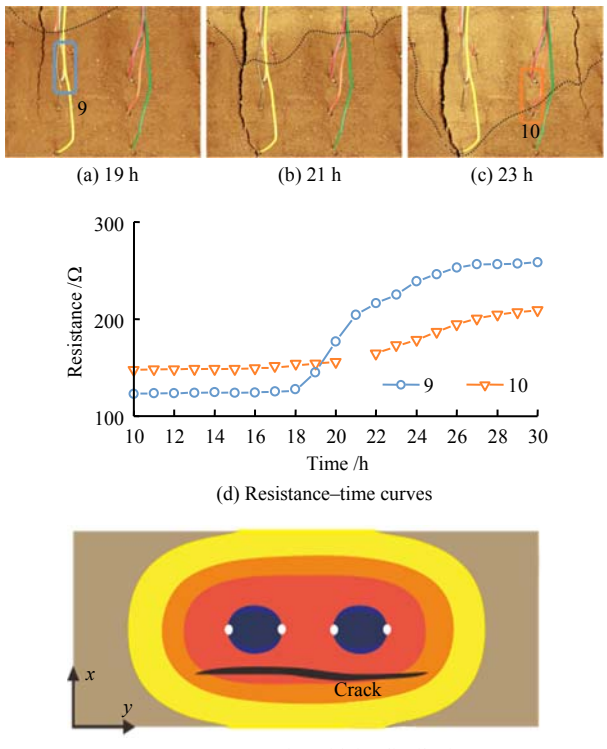

Fig. 8 Photos of the along-crack array, corresponding resistance curves and contour map of sensitivity distribution

3.2 Indoor natural desiccation crack network and interpreted resistivity analysis

The monitoring of the soil desiccation cracking process for the laboratory test lasted 63 h. The acquired

images showed that the development of the crack network was mainly from 16 h to 30 h. Therefore, the data from eight of the tests were selected for inversion at an interval of 2 h. The inversion followed the procedure described previously (Fig. 2).

The interpreted resistivity distributed discretely in the 3D space was obtained after inversion. The 8 × 8 array selected for data collection is not sensitive enough to detect deep soils due to the limited number of electrodes in each direction, thus the analysis focuses on the distribution of the interpreted resistivity in the surface soil. Data from the top 20 × 15 elements were selected to create the contour map of resistivity, and the growth path of crack was drawn based on the digital images (Fig. 9). Cracks did not appear until 16 h after the start of the test. Figure 9(a) indicates an average interpreted resistivity of approximately 30 Ω·m, but the distribution is not ideally uniform. This is because the contact between the soil and each electrode during shrinkage varies, leading to different test results for different electrode arrays. However, such differences do not significantly affect the subsequent crack characterization. Figure 9(b)–9(d) shows the initiation and propagation of the longitudinal cracks in the upper part of the picture, while Fig. 9(e)–9(h) shows the generation of other cracks and the general formation process of the crack network. High-resistivity zones (> 60 Ω·m) appear with the development of cracks. The formation and expansion of these high-resistivity zones obviously correspond to the formation and development of cracks, demonstrating the feasibility of monitoring on small-scale desiccation cracks with the ERT and confirming the reliability of the inversion algorithm.

The change rate of the interpreted resistivity at different stages relative to the initial crack-free state (Rev) is proposed as a more intuitive way to weaken the interference caused by poor electrode contact and to further highlight the effect of desiccation cracks on the electrical conductivity of soils, which is expressed by

$$\mathrm{Rev} = \frac{\rho_i - \rho_0}{\rho_0} \tag{3}$$

where ρ_0 is the interpreted resistivity distribution for the initial state; and ρ_i is the interpreted resistivity distribution for the state to be studied.

The eight groups of interpreted resistivity in Fig. 9 are calculated for Rev, where the values at 16 h were used as the initial state. The distribution of Rev at different times is shown in Fig. 10. As stated before, anomaly inversions will inevitably occur during the test and the initial inversion model is the apparent resistivity. The area close to the crack will still be inferred as low-resistivity zones where the interpreted resistivity is lower than the initial state, i.e. the Rev is negative. The minimum of the legend is set to 0 in the contour

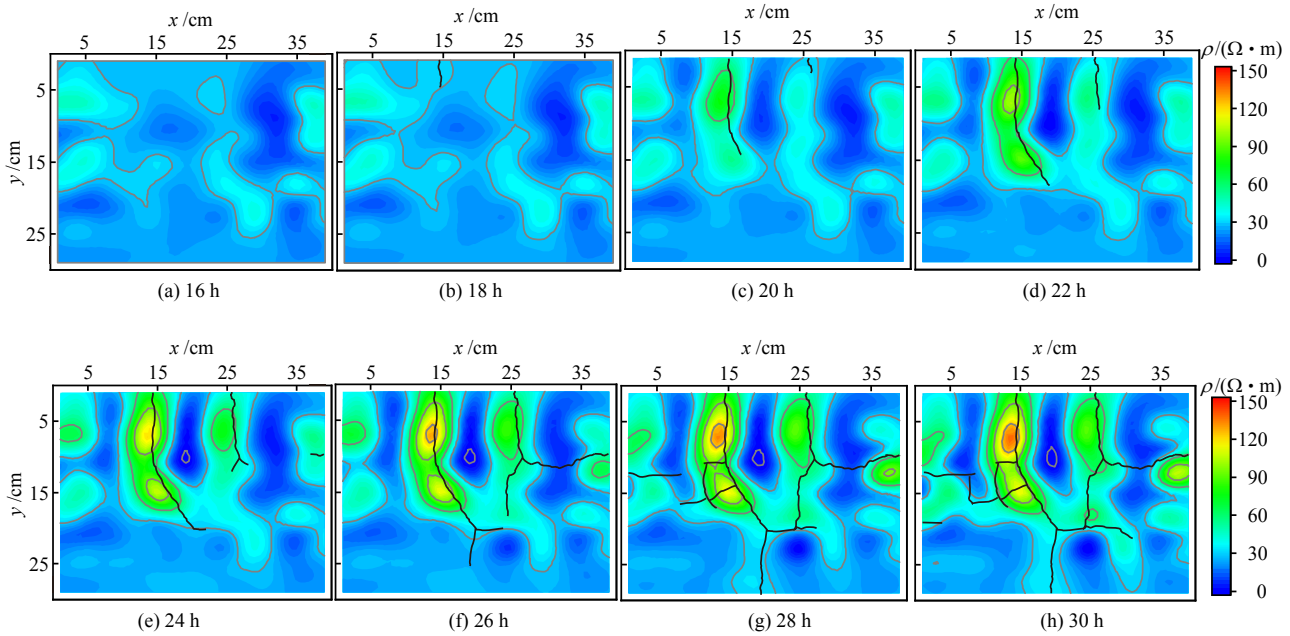

Fig. 9 Contour maps of the interpreted resistivity of soil surface (thick black lines are the main cracks)

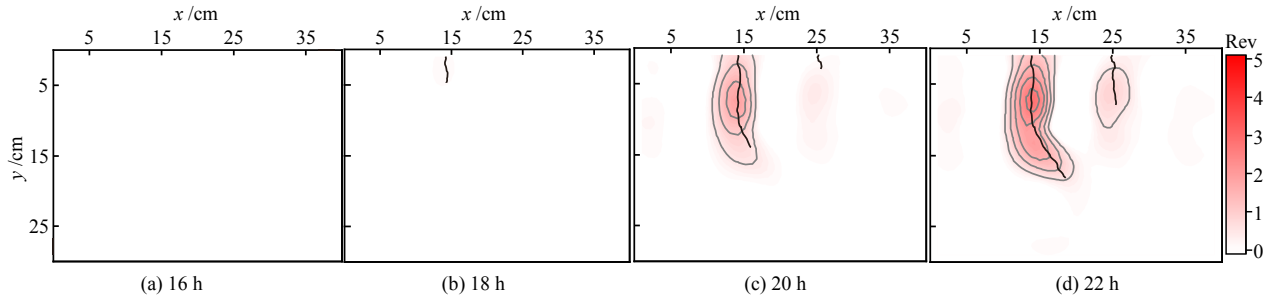

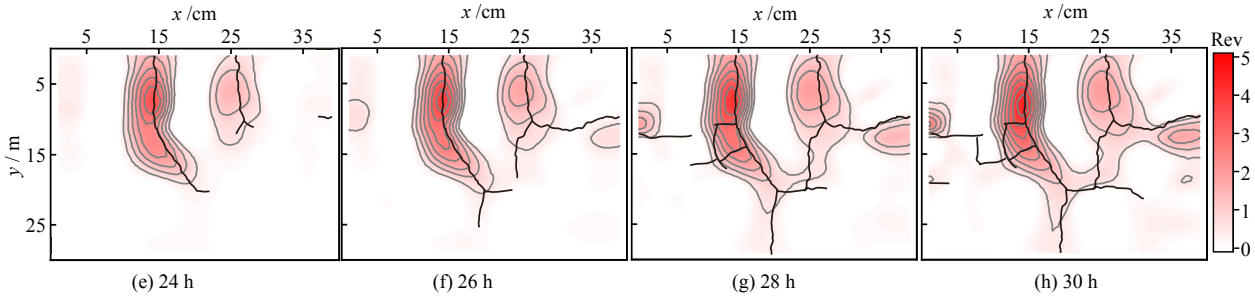

Fig. 10 Contour maps of the Rev of soil surface (thick black lines are the main cracks)

map to exclude the anomaly inversion. The Rev contour map is a better visual representation of the complete process of crack initiation and propagation than the interpreted resistivity contour map and will be used in the subsequent field test.

3.3 Field artificially simulated crack network and interpreted resistivity analysis

Figure 11 illustrates the resistivity distribution in the surface and profile of the soil at the initial stage and the final stage F. The resistivity at the initial stage averaged 40 Ω·m, with only a few areas above 50 Ω·m (Fig. 11(a)), due to the non-uniform soil and poor contact between individual electrodes and the soil. The continuous distribution of high-resistivity areas above 50 Ω·m in the soil surface and profile at stage F (Fig. 11(b)) is inferred as the effect of artificial cracks. Following the data processing procedure of the model test, the initial crack-free stage is selected as the initial state, and the Rev in the soil surface and profile at specific stages are analyzed. The dynamic characteristics of the longitudinal deepening and planar extension of the artificial crack network are discussed below.

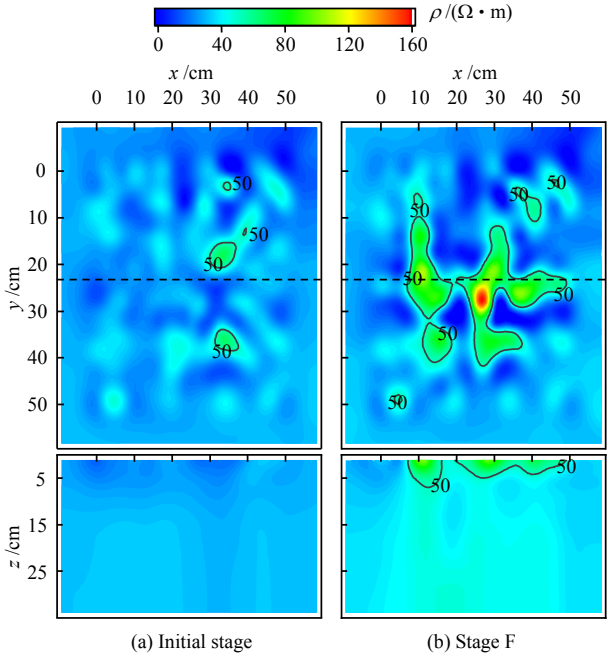

Fig. 11 Contour maps of the interpreted resistivity at the initial stage and the final stage F

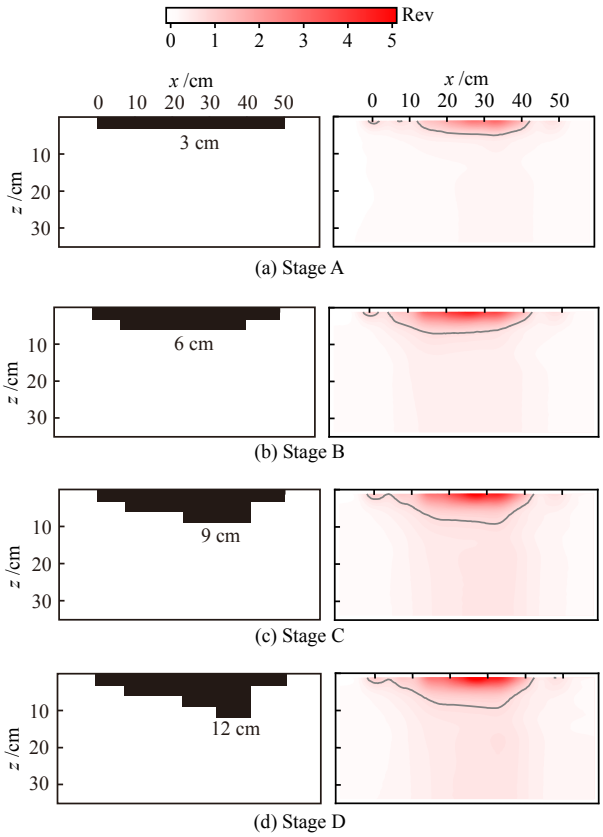

Fig. 12 Crack morphology and contour maps of the Rev of soil profile at stages A–D

The dynamic development along the depth is simulated at stages A–D of the field artificial cracks. Figure 12(a)–12(d) shows the crack geometric morphology and Rev distribution in the profile ($y = 23.3$ cm) at stages A–D, indicating a clear change of the Rev distribution as the crack propagates. The high Rev zone continuously expands deeper into the soil, and the grey contour of $\mathrm{Rev} = 0.7$ shows the geometric morphology of the crack in the profile. In fact, the Rev threshold for distinguishing between soils and cracks is influenced by the soil electrical conductivity, as well as the testing and inversion methods. The $\mathrm{Rev} = 0.7$ is only the optimal threshold that conforms to the actual morphology of the artificial crack. It is necessary to conduct a pre-test to determine a suitable Rev threshold for monitoring a site with unknown crack development. The contour variation reflects the crack deepening process in real time, indicating that the 3D

ERT monitoring also has a good detection capability for the dynamic crack development in the depth direction. Moreover, the small quantity of electrodes in this study has limited the detection capability for deeper soils. It is expected that a real-time quantitative assessment of crack depth using ERT will be possible when a more intensive electrode layout is carried out for the crack deepening process.

Figure 13 illustrates the distribution and change of Rev in the surface soil at stages D–F. The grey contour of Rev = 0.7 is also drawn to highlight the boundaries of the Rev anomaly zones. The areas with Rev above 0.7 match well with the planar geometric morphology of the crack network, further indicating that ERT is still effective in monitoring the crack network by weakening the non-uniformity of the initial state and the interference of poor individual electrode contact even in complex environmental conditions. The 3D ERT allows the refined simultaneous monitoring of the dynamic development process of the crack network and is expected to be implemented in engineering practice to obtain accurate geometric parameters of the desiccation crack network in real time.

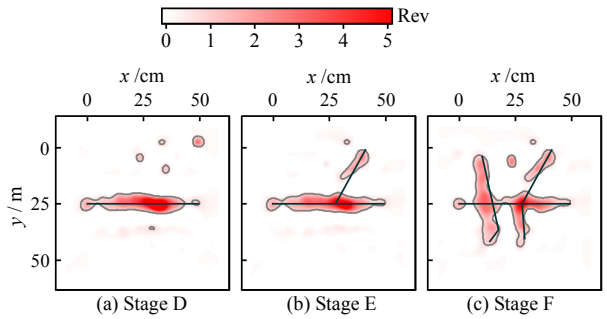

Fig. 13 Crack morphology and contour maps of the Rev of soil surface at stages D–F

4 Conclusions

A refined monitoring method based on the ERT is developed for the desiccation cracking process of soils, which is used to monitor the crack development process in the laboratory test and the field test. After the inversion by the FemERT system, the conclusions are summarized as follows:

(1) The difference in sensitivity distribution of the ERT can explain the effect of crack development on the electrical conductivity of the soil. The existence of cracks as high-resistivity bodies at different locations causes the different change patterns of the measured resistivity–time curves. Based on this, the development status of cracks at different times can be deduced.

(2) In the process of soil drying, the ERT data can visually characterize the planar geometric morphology of the millimeter-scale crack network at different stages after being inverted by the FemERT system. The change rate of the interpreted resistivity at different stages relative to the initial crack-free state (Rev) can be used to weaken the interference of other factors and further improve the accuracy of the ERT to characterize the geometrical morphology of the crack network.

(3) The interpreted resistivity can be adopted to characterize the development process of cracks in the depth direction, with an accuracy of centimeter level. The ERT proposed in this paper shows the potential of refined monitoring on the geometric morphology of the 3D crack networks and has broad application prospects in practical engineering such as embankment, slope and road.

Although the ERT is shown in this paper to be an efficient and non-destructive technical means for monitoring and evaluating the crack development in soils, it is believed that the future studies should focus on complex working conditions, further optimize the resistivity inversion algorithm, and construct quantitative relationships between interpreted resistivity and crack geometric parameters, for better application in engineering practice.

References

[1] IPCC. Climate change 2021: the physical science basis[M]. Cambridge: Cambridge University Press, 2021.

[2] JARDINE R J. Geotechnics, energy and climate change: the 56th Rankine Lecture[J]. Géotechnique, 2020, 70(1): 3–59.

[3] YAO Hai-lin, ZHENG Shao-he, CHEN Shou-yi. Analysis on the slope stability of expansive soils considering cracks and infiltration of rain[J]. Chinese Journal of Geotechnical Engineering, 2001, 23(5): 606–609.

[4] YIN Zong-ze, YUAN Jun-ping, WEI Jie, et al. Influence of fissures on slope stability of expansive soil[J]. Chinese Journal of Geotechnical Engineering, 2012, 34(12): 2155–2161.

[5] TANG C S, SHI B, LIU C, et al. Experimental characterization of shrinkage and desiccation cracking in thin clay layer[J]. Applied Clay Science, 2011, 52(1-2): 69–77.

[6] PERON H P, HUECKEL T H, LALOUI L L, et al. Fundamentals of desiccation cracking of fine-grained soils: experimental characterisation and mechanisms identification[J]. Canadian Geotechnical Journal, 2009, 46(10): 1177–1201.

[7] LUO Zhao-gang, WANG Shi-ji, YANG Zhen-bei. Quantitative analysis of fracture evolution of expansive soils under wetting-drying cycles[J]. Rock and Soil Mechanics, 2020, 41(7): 2313–2323.

[8] ALONSO E E, ROMERO E, HOFFMANN C, et al. Expansive bentonite-sand mixtures in cyclic controlled-suction drying and wetting[J]. Engineering Geology, 2005, 81(3): 213–226.

[9] TANG Chao-sheng, SHI Bin, LIU Chun. Study on desiccation cracking behaviour of expansive soil[J].

Journal of Engineering Geology, 2012, 20(5): 663–673.

[10] TANG Chao-sheng. Extreme climate engineering geology: soil engineering properties response to drought climate and measures for disaster mitigation[J]. Chinese Science Bulletin, 2020, 65(27): 3008–3027.

[11] TANG C S, ZHU C, CHENG Q, et al. Desiccation cracking of soils: a review of investigation approaches, underlying mechanisms, and influencing factors[J]. Earth-Science Reviews, 2021, 216: 103586.

[12] HU Dong-xu, LI Xian, ZHOU Chao-yun, et al. Quantitative analysis of swelling and shrinkage cracks in expansive soil[J]. Rock and Soil Mechanics, 2018, 39(Suppl.1): 318–324.

[13] WANG Zhi-guo, ZHOU Hong-wei, XIE He-ping. Research on fractal characterization of mined crack network evolution in overburden rock stratum under deep mining[J]. Rock and Soil Mechanics, 2009, 30(8): 2403–2408.

[14] SUN Kai-qiang, TANG Chao-sheng, LIU Chang-li, et al. Research methods of soil desiccation cracking behavior[J]. Rock and Soil Mechanics, 2017, 38(Suppl.1): 11–26.

[15] VELDE B. Structure of surface cracks in soil and muds[J]. Geoderma, 1999, 93(1): 101–124.

[16] YUAN Jun-ping, YIN Zong-ze. Quantitative index of fissure and strength characterisrics of fissured expansive soils[J]. Journal of Hydraulic Engineering, 2004(6): 108–113.

[17] DYER M, UTILI S, ZIELINSKI M. Field survey of desiccation fissuring of flood embankments[J]. Proceedings of the Institution of Civil Engineers- Water Management, 2009, 162(3): 221–232.

[18] LIN Zhu-yuan, TANG Chao-sheng, ZENG Hao, et al. Laboratory characterization and discrete element modeling of desiccation cracking behavior of soils under different boundary conditions[J]. Chinese Journal of Geotechnical Engineering, 2020, 42(2): 372–380.

[19] TANG C S, ZHU C, LENG T, et al. Three-dimensional characterization of desiccation cracking behavior of compacted clayey soil using X-ray computed tomography[J]. Engineering Geology, 2019, 255: 1–10.

[20] SANCHEZ M, ATIQUE A, KIM S, et al. Exploring desiccation cracks in soils using a 2D profile laser device[J]. Acta Geotechnica, 2013, 8(6): 583–596.

[21] CHENG Q, TANG C S, ZHU C, et al. Drying-induced soil shrinkage and desiccation cracking monitoring with distributed optical fiber sensing technique[J]. Bulletin of Engineering Geology and the Environment, 2020, 79(8): 3959–3970.

[22] SAMOUËLIAN A, COUSIN I, RICHARD G, et al. Electrical resistivity imaging for detecting soil cracking at the centimetric scale[J]. Soil Science Society of America Journal, 2003, 67(5): 1319–1326.

[23] SENTENAC P, ZIELINSKI M. Clay fine fissuring monitoring using miniature geo-electrical resistivity arrays[J]. Environmental Earth Sciences, 2009, 59(1): 205–214.

[24] JONES G, ZIELINSKI M, SENTENAC P. Mapping desiccation fissures using 3-D electrical resistivity tomography[J]. Journal of Applied Geophysics, 2012, 84: 39–51.

[25] JONES G, SENTENAC P, ZIELINSKI M. Desiccation cracking detection using 2-D and 3-D electrical resistivity tomography: validation on a flood embankment[J]. Journal of Applied Geophysics, 2014, 106: 196–211.

[26] TANG C S, WANG D Y, ZHU C, et al. Characterizing drying-induced clayey soil desiccation cracking process using electrical resistivity method[J]. Applied Clay Science, 2018, 152: 101–112.

[27] AN N, TANG C S, CHENG Q, et al. Application of electrical resistivity method in the characterization of 2D desiccation cracking process of clayey soil[J]. Engineering Geology, 2020, 265: 105416.

[28] GRIFFITHS D H, BARKER R D. Two-dimensional resistivity imaging and modelling in areas of complex geology[J]. Journal of Applied Geophysics, 1993, 29(3-4): 211–226.

[29] YAN Ya-jing, YAN Yong-shuai, ZHAO Gui-zhang, et al. Study on moisture migration in natural slope using high-density electrical resistivity tomography method[J]. Rock and Soil Mechanics, 2019, 40(7): 2807–2814.

[30] LI Zhu-dan, SUN Bo-yan, NONG Rui, et al. Imaging dry shrinkage cracks on farmland soil surface using electrical resistivity technology[J]. Transactions of the Chinese Society of Agricultural Engineering, 2022, 38(4): 105–112.

[31] TONKOV N, LOKE M H. A resistivity survey of a burial mound in the ‘Valley of the Thracian Kings’[J]. Archaeological Prospection, 2006, 13(2): 129–136.

[32] SENTENAC P, BENES V, BUDINSKY V, et al. Post flooding damage assessment of earth dams and historical reservoirs using non-invasive geophysical techniques[J]. Journal of Applied Geophysics, 2017, 146: 138–148.

[33] ZHOU Q Y, SHIMADA J, SATO A. Three-dimensional spatial and temporal monitoring of soil water content using electrical resistivity tomography[J]. Water Resources Research, 2001, 37(2): 273–285.

[34] SAMOUËLIAN A, RICHARD G, COUSIN I, et al. Three-dimensional crack monitoring by electrical resistivity measurement[J]. European Journal of Soil Science, 2004, 55(4): 751−762.

[35] GREVE A K, ACWORTH R I, KELLY B F J. Detection of subsurface soil cracks by vertical anisotropy profiles of apparent electrical resistivity[J]. Geophysics, 2010, 75(4): WA85−WA93.

[36] KONG L-W, BAI W, GUO A-G. Effects of cracks on the electrical conductivity of a fissured laterite: a combined experimental and statistical study[J]. Geotechnical Testing Journal, 2012, 35(6): 870−878.

[37] WU H, CHIU C. Detecting depth of desiccation-induced clay crack based on anisotropy index (AI) of apparent electrical resistivity[J]. Converter, 2021, 2021(7): 590−603.

[38] ZHOU Q Y. A sensitivity analysis of DC resistivity prospecting on finite, homogeneous blocks and columns[J]. Geophysics, 2007, 72(6): 237−247.

[39] ZHOU Q Y, SHIMADA J, SATO A. Three-dimensional soil resistivity inversion using patching method[J]. Journal of the Japan Society of Engineering Geology, 1999, 39(6): 524−532.

[40] ZHOU Q Y, MATSUI H, SHIMADA J. Characterization of the unsaturated zone around a cavity in fractured rocks using electrical resistivity tomography[J]. Journal of Hydraulic Research, 2004, 42(Suppl.1): 25−31.

[41] LIU Ting-fa, NIE Yan-xia, HU Li-ming, et al. Model tests on moisture migration based on high-density electrical resistivity tomography method[J]. Chinese Journal of Geotechnical Engineering, 2016, 38(4): 761−768.

[42] LOKE M H. Tutorial : 2-D and 3-D electrical imaging surveys [M/OL]. [S. l.]: [s. n.], 2004: 31-32 [2021-08-27]. http://www. geotomosoft.com.

[43] ACKERSON J P, MORGAN C L S, EVERETT M E, et al. The role of water content in electrical resistivity tomography of a vertisol[J]. Soil Science Society of America Journal, 2014, 78(5): 1552−1562.

[44] GANCE J, SAILHAC P, MALET J-P. Corrections of surface fissure effect on apparent resistivity measurements[J]. Geophysical Journal International, 2015, 200(2): 1118−1135.

[45] ARCHIE G E. The electrical resistivity log as an aid in determining some reservoir characteristics[J]. Transactions of the AIME, 1942, 146(1): 54−62.